Proceedings of ASME FEDSM'00
ASME 2000 Fluids Engineering Division Summer Meeting
Boston, Massachusetts, June 11-15, 2000

FEDSM2000-11197

VISUALIZATION OF SHEAR STRESS WITH MICRO IMAGING CHIP AND DISCRETE WAVELETS TRANSFORM

Masahiro TAKEI Motoaki KIMURA
Department of Mechanical Engineering
College of Science and Technology, Nihon Univ.
Tokyo, Japan
takei@mech.cst.nihon-u.ac.jp

Yoshifuru SAITO
Department of Electrical & Electronic Engineering
College of Technology, Hosei University
Tokyo Japan

Chih-Ming HO
Mechanical and Aerospace Engineering Department
University of California, Los Angeles
Los Angeles, California, USA

Kiyoshi HORII
Shirayuri College
Tokyo Japan

Keywords: Discrete Wavelets Transform, Frequency Analysis, Turbulent Flow, Boundary Layer, MEMS, Shear Stress Sensor

ABSTRACT

Two dimensional stripe structure in turbulent boundary layer has been clearly visualized by a combination of a shear stress sensor using MEMS (Micro-Electro-Mechanical-Systems) and discrete wavelets transform. The MEMS shear stress micro chip is designed and fabricated by surface micro-machining technology, contributing to obtaining the time-space two dimensional shear stress data. The discrete wavelets transform is a software technique to decompose the frequency level with the time and space information of the wave form. The experiments for the shear stress distribution were carried out on Re = 6960, 12180 and 17400. This technique for a single phase flow is applicable to multiphase flow analysis.

INTRODUCTION

Our research group has been studying a spiral multiphase flow which is a swirling flow with a large free vortex region, a high concentration to the axis and high stability [Horii 1990]. From the characteristics, the spiral flow is useful for a high performance pneumatic transportation without particles touching pipe inner wall due to the stable eddy structure [Takei 1997]. Accordingly, it is necessary to analyze near-wall shear stress of the solid-air two phase flow to improve the system because the particle stability in solid-air pipeline is affected by eddy structure due to shear stress which occurs near the wall.

The presence of near-wall shear stress streaks in turbulent boundary layer has been observed for many years in flow visualization and experimental investigation [Cantwell 1891, Kim H. T 1971, Falco 1980, Head 1981, Smith 1983]. At high Reynolds numbers, these streaks are typically very small in size and cannot be properly resolved by traditional measuring techniques. Numerical simulations indicate that the streaks are associated with streamwise vortices in the viscous sub-layer. The rotational motion of these vortices imposes high fluctuating surface shear stress on the wall [Kim, J. 1987]. There have been many measurement techniques for measuring shear stress. The hot-film technique and its variants have been widely used for the detailed investigations of fluctuating wall shear stress [Alfredsson 1988, Bruun 1995]. The direction sensitive laser Doppler anemometer is a candidate, which enables to evaluate both magnitude and direction of the wall shear stress. An optical method proposed by Naquwi is supposed to be capable of measuring the wall shear stress with high spatial resolution [Naquwi and Reynolds 1991]. No matter the instrument, the requirements of fine spatial resolution, fast frequency response, high sensitivity and convenience need to be satisfied for turbulent boundary layer research.

Recently, the availability of a new manufacturing process, micro-electro-mechanical-systems (MEMS) technology, has offered the possibility of sensing and controlling the small near-wall streaks [Ho 1997]. A multidisciplinary research collaboration between UCLA and Caltech has undergone to design and fabricate a large-scale distributed control system with integrated micromachined transducers and microelectronic

circuits for surface shear stress control in turbulent boundary layers [Tung 1995, Ho 1996].

However, the distribution of stripe structure with MEMS is the integral value that is composed of various kinds of frequency ingredients. It leads to make the stripe structure ambiguous. Therefore, new techniques such as statistics analysis and frequency analysis to the image data is necessary for analyzing the structure in details. The stripe structure obtained with the micro imaging chip is clearly visualized with the statistics method [Kimura 1997]. In terms of the frequency analysis, Fourier transform is a popular method; however, the transform removes the time and space information of the stripe structure.

Currently, wavelets transform has been started using for time-space frequency analysis instead of Fourier transform in mechanical engineering fields. The merits of the wavelets analysis is to be able to analyze the frequency not to erase the time-space information. Wavelets transform [Moret 1989] is roughly classified with two types, which are continuous wavelets transform and discrete wavelets transform. The ntinuous wavelets transform has been generally used for time requency analysis in vibration wave. For example, self-similarity of a jet inner structure [Everson 1990], breakdown of a large eddy and successive branching in a plane jet [Li 1995], decomposition of Reynolds stress in a jet [Gordeyev 1995], and multiple acoustic modes and shear layer instability [Walker 1995] were investigated. However, most of the researchers on the time-frequency analysis carried out the continuous wavelets transform. On the other hand, the discrete wavelets transform has been mainly used for picture image processing. The analysis enables to decompose and to compose picture image data quantitatively because of the orthonormal transform. Saito applied this idea to analyzing electromagnetic wave[Saito 1996].

The originality of this paper lies in applying discrete wavelets transform to visualizing the wall shear stress obtained with micro shear stress imaging chip. In this study, the stripe structure of shear stress in a turbulence boundary layer are extracted on various frequency levels with discrete wavelets nsform.

THEORY OF DISCRETE WAVELETS TRANSFORM

Basic Concept Using Simple Base Function

Basic concept of discrete wavelets transform is described using matrix expression instead of integral expression. One dimensional input data matrix with four elements **X** and an analyzing wavelets matrix of Haar base function **W** are used to simplify the expression. For example, the input data matrix **X** is one dimensional shear stress data. The wavelets transform matrix **S** that indicates wavelets spectrum is expressed by

$$\begin{bmatrix} S_1 \\ D_1 \\ d_1 \\ d_2 \end{bmatrix} = \left(\frac{1}{\sqrt{2}}\right)^2 \begin{bmatrix} 1 & 1 & 1 & 1 \\ 1 & 1 & -1 & -1 \\ \sqrt{2} & -\sqrt{2} & 0 & 0 \\ 0 & 0 & \sqrt{2} & -\sqrt{2} \end{bmatrix} \begin{bmatrix} a \\ b \\ c \\ d \end{bmatrix} \quad \text{——(1)}$$

or $\mathbf{S} = \mathbf{W} \cdot \mathbf{X}$ ——(2)

Where, $\mathbf{W}^T \cdot \mathbf{W} = \mathbf{I}$, **I** is a unit matrix and $\mathbf{W}^T$ is a transpose matrix of **W**. The analyzing wavelets matrix is an orthonormal. In Eq. (1), the first element in the wavelets spectrum S_1 shows a transform to obtain a mean value with a weight on the all input data, $a+b+c+d$. The second element in the wavelets spectrum D_1 shows a transform to obtain a difference value between the fast half and the latter half with a weight on the input data, $\{(a+b)-(c+d)\}$. It means that this element includes the lower frequency level of the input data. The third element d_1 shows a transform to obtain a difference value on the first half of the input data, $(a-b)$. The fourth element d_2 is a transform to obtain a difference value on the latter half, $(c-d)$. The third and forth elements include the higher frequency level of the input data. Therefore, the input data is able to classified to a range from higher frequency level to lower frequency level. Because of the orthonormal function, the inverse discrete wavelets transform is expressed by,

$$\mathbf{X} = \mathbf{W}^T \cdot \mathbf{S} \quad \text{——(3)}$$

Moreover, from Eq.(3), the input data **X** is decomposed by multiresolution. The matrix expression is

$$\begin{bmatrix} a \\ b \\ c \\ d \end{bmatrix} = \left(\frac{1}{\sqrt{2}}\right)^2 \begin{bmatrix} 1 & 1 & \sqrt{2} & 0 \\ 1 & 1 & -\sqrt{2} & 0 \\ 1 & -1 & 0 & \sqrt{2} \\ 1 & -1 & 0 & -\sqrt{2} \end{bmatrix} \begin{bmatrix} S_1 \\ D_1 \\ d_1 \\ d_2 \end{bmatrix} = \mathbf{W}^T \begin{bmatrix} S_1 \\ 0 \\ 0 \\ 0 \end{bmatrix} + \mathbf{W}^T \begin{bmatrix} 0 \\ D_1 \\ 0 \\ 0 \end{bmatrix} + \mathbf{W}^T \begin{bmatrix} 0 \\ 0 \\ d_1 \\ d_2 \end{bmatrix} \quad \text{——(4)}$$

or $\mathbf{X} = \mathbf{W}^T\mathbf{S} = \mathbf{W}^T\mathbf{S}_0 + \mathbf{W}^T\mathbf{S}_1 + \mathbf{W}^T\mathbf{S}_2$ ——(5)

Where, $\mathbf{S}_0 = [S_1\ 0\ 0\ 0]^T$ $\mathbf{S}_1 = [0\ D_1\ 0\ 0]^T$ $\mathbf{S}_2 = [0\ 0\ d_1\ d_2]^T$. $\mathbf{W}^T\mathbf{S}_0$, $\mathbf{W}^T\mathbf{S}_1$ and $\mathbf{W}^T\mathbf{S}_2$ are called Level 0, Level 1 and Level 2, respectively.

Generalization of Discrete Wavelets Transform

Many orthonormal wavelets analyzing functions are found [Molet 1989]. The basic concept of the discrete wavelets transform is generalized by using fourth Daubechies function. The analyzing wavelets matrix is also an orthonormal function. The analyzing wavelets matrix **W** is acquired by a cascade algorithm on the basis of a function matrix **C**. The matrix **C** is shown in Eq.(6),

$$\mathbf{C} = \begin{pmatrix} c_0 & c_1 & c_2 & c_3 & 0 & 0 & \cdots & 0 & 0 & 0 & 0 \\ c_3 & -c_2 & c_1 & -c_0 & 0 & 0 & \cdots & 0 & 0 & 0 & 0 \\ 0 & 0 & c_0 & c_1 & c_2 & c_3 & \cdots & 0 & 0 & 0 & 0 \\ 0 & 0 & c_3 & -c_2 & c_1 & -c_0 & \cdots & 0 & 0 & 0 & 0 \\ \vdots & & & & & & & & & & \\ 0 & 0 & 0 & 0 & 0 & 0 & \cdots & c_0 & c_1 & c_2 & c_3 \\ 0 & 0 & 0 & 0 & 0 & 0 & \cdots & c_3 & -c_2 & c_1 & -c_0 \\ c_2 & c_3 & 0 & 0 & 0 & 0 & \cdots & 0 & 0 & c_0 & c_1 \\ c_1 & -c_0 & 0 & 0 & 0 & 0 & \cdots & 0 & 0 & c_3 & -c_2 \end{pmatrix} \begin{matrix} c_0 = \frac{1+\sqrt{3}}{4\sqrt{2}} \\ c_1 = \frac{3+\sqrt{3}}{4\sqrt{2}} \\ c_2 = \frac{3-\sqrt{3}}{4\sqrt{2}} \\ c_3 = \frac{1-\sqrt{3}}{4\sqrt{2}} \end{matrix} \quad \text{——(6)}$$

$c_3 - c_2 + c_1 - c_0 = 0$ ——(7) $0\,c_3 - 1\,c_2 + 2\,c_1 - 3\,c_0 = 0$ ——(8)

Where, $\mathbf{C}^T \cdot \mathbf{C} = \mathbf{I}$. The first line in Eq.(6) is called scaling coefficients and second line is called wavelets coefficients. Forth Daubechies function has four coefficients in a line. The first line shows a transform to obtain a mean value with weights of c_0, c_1, c_2 and c_3 on the input data. The second line shows a

transform to obtain a difference value with weights of c_0, c_1, c_2 and c_3 on the input data. The third line shows a transform to translate the first line by two steps. The fourth line is a transform to do the second line by two steps. Eqs.(7) and (8) show the transformed values are zero when the input data are constant or are simply increased. To explain easily the process to acquire the analyzing wavelets matrix **W** from **C**, the matrix **X** is assumed to be one dimensional 16 elements,

$$\mathbf{X} = [x_1\ x_2\ x_3\ x_4\ x_5\ x_6\ x_7\ x_8\ x_9\ x_{10}\ x_{11}\ x_{12}\ x_{13}\ x_{14}\ x_{15}\ x_{16}]^T \quad \text{——(9)}$$

From Eqs. (6) and (9), the transformed matrix **X'** is

$$\mathbf{X'} = \mathbf{C_{16}X} = [s_1\ d_1\ s_2\ d_2\ s_3\ d_3\ s_4\ d_4\ s_5\ d_5\ s_6\ d_6\ s_7\ d_7\ s_8\ d_8\ ]^T \quad \text{——(10)}$$

Where, $\mathbf{C_{16}}$ is 16X16 matrix of **C**. The element s indicates the mean value and the element d indicates the difference value. The elements in the matrix **X'** are replaced by a matrix $\mathbf{P_{16}}$.

$$\mathbf{P_{16}X'} = \mathbf{P_{16}}\ \mathbf{C_{16}X} = [s_1\ s_2\ s_3\ s_4\ s_5\ s_6\ s_7\ s_8\ d_1\ d_2\ d_3\ d_4\ d_5\ d_6\ d_7\ d_8\ ]^T \text{—(11)}$$

Where, $\mathbf{P_{16}}$ is defined as

$$\mathbf{P_{16}} = \begin{pmatrix}
1&0&0&0&0&0&0&0&0&0&0&0&0&0&0&0\\
0&0&1&0&0&0&0&0&0&0&0&0&0&0&0&0\\
0&0&0&0&1&0&0&0&0&0&0&0&0&0&0&0\\
0&0&0&0&0&0&1&0&0&0&0&0&0&0&0&0\\
0&0&0&0&0&0&0&0&1&0&0&0&0&0&0&0\\
0&0&0&0&0&0&0&0&0&0&1&0&0&0&0&0\\
0&0&0&0&0&0&0&0&0&0&0&0&1&0&0&0\\
0&0&0&0&0&0&0&0&0&0&0&0&0&0&1&0\\
0&1&0&0&0&0&0&0&0&0&0&0&0&0&0&0\\
0&0&0&1&0&0&0&0&0&0&0&0&0&0&0&0\\
0&0&0&0&0&1&0&0&0&0&0&0&0&0&0&0\\
0&0&0&0&0&0&0&1&0&0&0&0&0&0&0&0\\
0&0&0&0&0&0&0&0&0&1&0&0&0&0&0&0\\
0&0&0&0&0&0&0&0&0&0&0&1&0&0&0&0\\
0&0&0&0&0&0&0&0&0&0&0&0&0&1&0&0\\
0&0&0&0&0&0&0&0&0&0&0&0&0&0&0&1
\end{pmatrix} \quad \text{——(12)}$$

Moreover, from Eq.(11), the transform is continuously carried out by **C** and **P** without any operations to the difference values,

$$\mathbf{W^{(2)}X} = [S_1\ S_2\ S_3\ S_4\ D_1\ D_2\ D_3\ D_4\ d_1\ d_2\ d_3\ d_4\ d_5\ d_6\ d_7\ d_8]^T \quad \text{——(13)}$$

$$\mathbf{S} = \mathbf{W^{(3)}X} = [S_1\ S_2\ D_1\ D_2\ D_1\ D_2\ D_3\ D_4\ d_1\ d_2\ d_3\ d_4\ d_5\ d_6\ d_7\ d_8]^T \text{—(14)}$$

Where,

$$\mathbf{W^{(2)}} = (\mathbf{P_{16}'C'_{16}})(\mathbf{P_{16}C_{16}}) \quad \text{——(15)}$$

$$\mathbf{W^{(3)}} = (\mathbf{P_{16}''\ C_{16}''})(\mathbf{P_{16}'\ C_{16}'})(\mathbf{P_{16}C_{16}}) \quad \text{——(16)}$$

$$\mathbf{P_{16}'} = \begin{bmatrix} \mathbf{P_8} & \mathbf{0} \\ \mathbf{0} & \mathbf{I_8} \end{bmatrix} \mathbf{C_{16}'} = \begin{bmatrix} \mathbf{C_8} & \mathbf{0} \\ \mathbf{0} & \mathbf{I_8} \end{bmatrix} \mathbf{P_{16}''} = \begin{bmatrix} \mathbf{P_4} & \mathbf{0} \\ \mathbf{0} & \mathbf{I_{12}} \end{bmatrix} \mathbf{C_{16}''} = \begin{bmatrix} \mathbf{C_4} & \mathbf{0} \\ \mathbf{0} & \mathbf{I_{12}} \end{bmatrix} \quad \text{—(17)}$$

$\mathbf{W^{(3)}}$ is a analyzing wavelets matrix that is **W** in Eq.(2). The wavelets spectrum **S** in Eq.(2) is $\mathbf{W^{(3)}X}$ in Eq. (14). In Eq.(13), S_1 indicates the mean value from s_1 to s_4 in Eq.(11). S_2 indicates the mean value from s_3 to s_6 that translate by two steps. D_1 indicates the difference value from s_1 to s_4. In Eq.(14), S_1 indicates the mean value from S_1 to S_4 in Eq.(13). D_1 indicates the difference value from S_1 to S_4 in Eq.(13). From Eq.(14), the input data are transformed to the mean values and the difference values with valuable resolution levels by the discrete wavelets transform. The input data are divided into a range from high frequency to low frequency.

From Eq.(14), the inverse wavelets transform is,

$$\mathbf{X} = [\mathbf{W^{(3)}}]^T\mathbf{S} \quad \text{——(18)}$$

$$[\mathbf{W^{(3)}}]^T = [(\mathbf{P_{16}''C_{16}''})(\mathbf{P_{16}'C_{16}'})(\mathbf{P_{16}C_{16}})]^T$$

$$= \mathbf{C_{16}}^T\mathbf{P_{16}}^T(\mathbf{C_{16}'})^T(\mathbf{P_{16}'})^T(\mathbf{C_{16}''})^T(\mathbf{P_{16}''})^T \quad \text{——(19)}$$

From Eq.(18), the multiresolution is,

$$\mathbf{X} = [\mathbf{W^{(3)}}]^T\mathbf{S} = [\mathbf{W^{(3)}}]^T\mathbf{S_0} + [\mathbf{W^{(3)}}]^T\mathbf{S_1} + [\mathbf{W^{(3)}}]^T\mathbf{S_2} + [\mathbf{W^{(3)}}]^T\mathbf{S_3} \quad \text{——(20)}$$

Where,

$$\mathbf{S_0} = [S_1\ S_2\ 0\ 0\ 0\ 0\ 0\ 0\ 0\ 0\ 0\ 0\ 0\ 0\ 0\ 0]^T$$

$$\mathbf{S_1} = [0\ 0\ D_1\ D_2\ 0\ 0\ 0\ 0\ 0\ 0\ 0\ 0\ 0\ 0\ 0\ 0]^T$$

$$\mathbf{S_2} = [0\ 0\ 0\ 0\ D_1\ D_2\ D_3\ D_4\ 0\ 0\ 0\ 0\ 0\ 0\ 0\ 0]^T$$

$$\mathbf{S_3} = [0\ 0\ 0\ 0\ 0\ 0\ 0\ 0\ d_1\ d_2\ d_3\ d_4\ d_5\ d_6\ d_7\ d_8]^T \quad \text{——(21)}$$

In the case of sixteen input data and fourth Daubechies, multiresolution indicates from Level 0 to Level 3.

The two dimensional wavelets spectrum **S** is obtained from

$$\mathbf{S} = \mathbf{W_n} \cdot \mathbf{X} \cdot \mathbf{W_m}^T \quad \text{——(22)}$$

Where, $\mathbf{W_m}^T$ is a transpose matrix of $\mathbf{W_n}$. From Eq.(22), the discrete inverse wavelets transform is expressed by

$$\mathbf{X} = \mathbf{W_n}^T \cdot \mathbf{S} \cdot \mathbf{W_m} \quad \text{——(23)}$$

In general, in the case that input data is 2^n and Daubechies function is kth, the algorithm to obtain the frequency levels is shown in Fig.1. The final wavelets spectrum is obtained after the wavelets transform in Eq.(14) continues until the number of final summation elements is less than k.

In this study, 16th Daubechies function is used instead of the fourth Daubechies function that is explained the above as analyzing wavelets. Scaling coefficients of the first line in Eq.(6) are shown in Fig.2. The fundamental properties are similar to fourth Daubechies function. In the case that 16th Daubechies function and the space data number 32 (all space 9.6mm; pseudo-space are included) and the time data number 512 (all measurement time 51.2ms), the wavelets level of the multiresolution is decomposed from level 0 to level 6 in the time, and from level 0 to level 3 in the space.

The absolute values by Fourier transform to the analyzing wavelets of this case are shown in Fig.3 and Fig.4. The each level operates a kind of band pass filter.

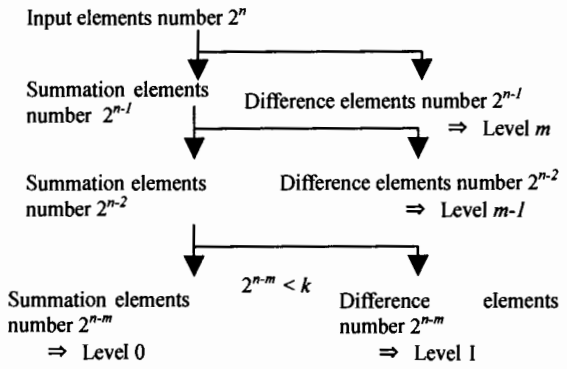

Fig. 1 Algorithm of discrete wavelets transform

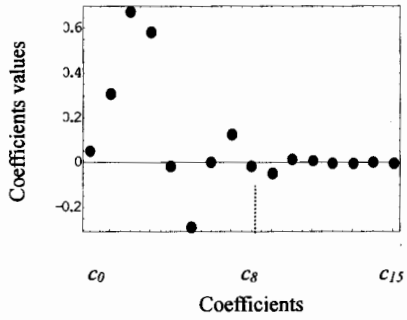

Fig.2 Coefficients of sixteenth Daubechies

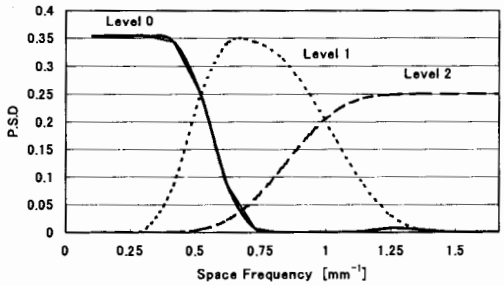

Fig.3 Space frequency of sixteenth Daubechies

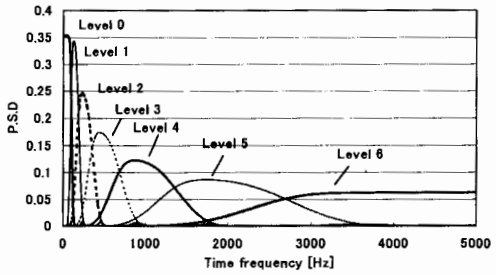

Fig.4 Time frequency of sixteenth Daubechies

EXPERIMENTS

Micro Shear Stress Imaging Chip

A micro shear-stress imaging chip, which is composed of multiple thermal type sensors [Jiang et al. 1996], is shown in Fig.5. The imaging chip has three rows of micro sensors, which ontain an array of 25 sensors. Fig. 6 shows a top and a cross sections of the micro shear stress sensor. Each micro sensor consists of a 150 μm long, 3 μm wide and 0.45 μm thick polysilicon resistor wire, and a 1.2 μm thick and 200 x 200 μm^2 silicon nitride diaphragm that seals off a 2 μm deep vacuum cavity underneath. The purposes of the cavity are to reduce heat transfer from the resistor wire to the substrate and to increase the sensitivity of the sensor [Huang et al. 1996]. The sensors are connected to external constant temperature mode circuits which are used in a hot-wire anemometer, to drive at a 1.1 overheat ratio, through gold bonding wires. Output from the anemometer circuits is digitized by a 64-channel Keithly Metrabyte ADC board in a Pentium based PC. The sensitivity of the shear stress sensor is about 1.0 V/Pa with a frequency response of 25 kHz at a 10 gain.

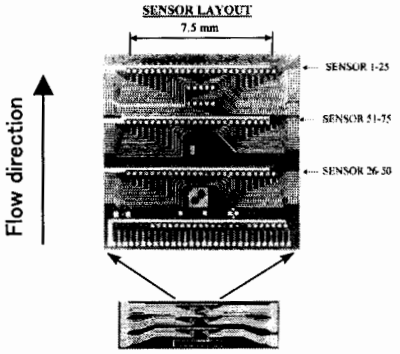

Fig.5 A surface shear stress imaging chip

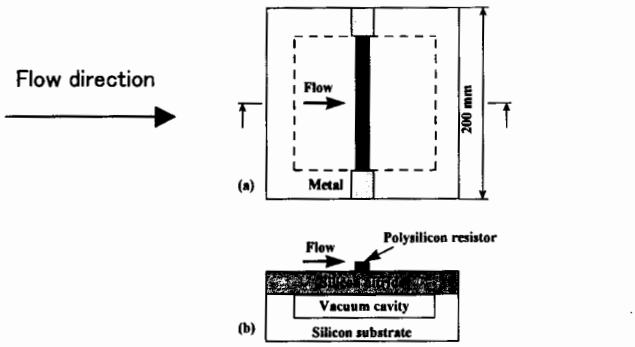

Fig.6 Schematic top (a) and cross-sectional (b) views of the micro shear stress sensor

Experimental Setup

This experiment was carried out in a turbulent channel flow facility. The channel, constructed of 13 mm Plexiglas, is 610 mm x 25.4 mm in a cross-section and 4880 mm long. An axial blower controlled by a DC power generates the air flow in the channel. Previous hot-wire measurement indicates that the channel flow, at a centerline velocity of 10 m/s, consists of a laminar entrance flow and a fully developed turbulent flow at the downstream half channel. The micro shear stress imaging chip was flush mounted into the wall at 4267 mm from the channel inlet where a fully developed turbulent channel flow exists. One array consisting of 25 micro shear-stress sensors that covers a 7.5 mm distance measures the instantaneous spanwise distribution of the turbulent surface shear stress. The *Re* number ($=hu_\infty/\nu$, where h is half width of the channel, u_∞ is centerline velocity) ranged from 6,960 to 17,400.

Shear-Stress Distribution

Statistics values of a wall shear stress measured by this imaging chip are confirmed [Kimura 1999] to be similar to the data obtained by the previous experiments [Obi 1995] [Alfredson 1998], and those by the numerical computation [Kim 1987]. Fig.7 shows the contour of 2-D shear stress distributions measured by the imaging chip. The horizontal axis covers a 7.5 mm wide area (data number 25), and the vertical axis dose

512.2 ms area in time (data number 512) in three different *Re* numbers. Each shear stress is normalized by

$$\bar{\tau} = \frac{\tau - \tau_{min}}{\tau_{max} - \tau_{min}} \qquad \text{—(24)}$$

using the maximum value τ_{max} and minimum value τ_{min} in each Reynolds number as shown in these figures (a), (b) and (c). In other words, the shear stress values are normalized with the minimum value 0.0 and the maximum value 1.0 in each *Re* number. The areas with high shear stress are marked by light-gray while dark-gray represents low shear stress with 11 contour colors. Fig.7(d) indicates the original data before the normalization in vertical direction at the point where maximum τ_{max} appears. From Fig.7(d), the transverse scale of the longitudinal high shear-stress streaks varies with *Re* numbers. The streaks are narrower and packed more densely as *Re* number increases. They also appear at the shorter time interval as *Re* number increase. The shear stress fluctuation near wall increases rapidly, resulting in a steep peak in a turbulence boundary layer, because a velocity gradient is rapidly increases due to the influence of eddy guided by bursting events. From Fig.7(a) to (c), an area of a white part (a relatively large value) in *Re*=17400 is smaller and an area of a black part (a comparatively small value) is larger than the lower *Re* number. The peak of shear stress is smoothed in *Re* number because the areas are normalized with the maximum and minimum values.

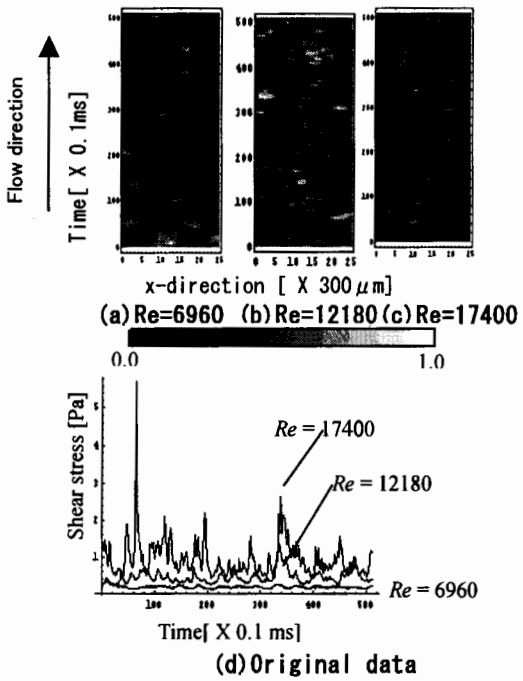

Fig.7 Shear stress measured with the imaging chip

ANALYSIS AND DISCUSSION

Analysis Method

The multiresolution analysis is carried out to the wavelets spectrum by the inverse wavelets transform in Eq.(23), after the wavelets transform in Eq.(22) is operated to 25x512 shear stress distribution data in Fig.7. Zero is put into the matrix position from 26 to 32 in x coordinate in Fig.7 intentionally because the data number of discrete wavelets transform is subject to nth power of two. In the case of sixteenth Daubechies function and 512 (=2^9) input data, the multiresolution classifies to seven levels as shown in

$$\mathbf{X} = [\mathbf{W}_n^{(5)}]^T \cdot \mathbf{S} \cdot [\mathbf{W}_m^{(5)}] = [\mathbf{W}_n^{(5)}]^T \cdot \mathbf{S}_0 \cdot [\mathbf{W}_m^{(5)}] + [\mathbf{W}_n^{(5)}]^T \cdot \mathbf{S}_1 \cdot [\mathbf{W}_m^{(5)}] + [\mathbf{W}_n^{(5)}]^T \cdot \mathbf{S}_2 \cdot [\mathbf{W}_m^{(5)}] + [\mathbf{W}_n^{(5)}]^T \cdot \mathbf{S}_3 \cdot [\mathbf{W}_m^{(5)}] + [\mathbf{W}_n^{(5)}]^T \cdot \mathbf{S}_4 \cdot [\mathbf{W}_m^{(5)}] + [\mathbf{W}_n^{(5)}]^T \cdot \mathbf{S}_5 \cdot [\mathbf{W}_m^{(5)}] + [\mathbf{W}_n^{(5)}]^T \cdot \mathbf{S}_6 \cdot [\mathbf{W}_m^{(5)}] \qquad \text{—(25)}.$$

$\mathbf{W}^{(5)}$ indicates the five times operation to obtain Daubechies matrix from a matrix **C** in Eq.(6). The values from 1 to 25 in x coordinate are extracted after the calculation.

Analysis Results

Figs.8, 9 and 10 (see the final page) show the multiresolution with 11 contours in the low *Re* number, the middle *Re* number and the high *Re* number, respectively. The low shear stress is shown with black, the high shear stress is shown with white from -0.2 to 0.4. The minus values are produced because they are normalized beforehand with the minimum value 0.0. Level 6 is not shown because the noise is dominant. The patterns adding all levels from Level 0 to Level 6 recover completely the original shear stress distributions in Fig.7, because Daubechies analyzing wavelets are orthonormal functions. The relation between the representative frequency, which is calculated with the maximum P.S.D. in Figs.3 and 4, and each wavelets level is shown in Table 1. From these figures, the original input data are decomposed from a low frequency component Level 0 to a high frequency component Level 5. The stripe structures due to a series of bursting events in the low speed shear stress area are visualized clearly on each frequency level without erasing the time and space information. In particular, the light and shade appear more clearly on Levels 0 and 1 in low *Re* number than high *Re* number. The shear stress distribution appears until Level 3; however, the wave pattern shades on Levels 4 and 5.

Table 1 Relation between wavelets level and representative frequency

	Time frequency	Space frequency
Representative frequency on Level 0	2.0 $\times 10^1$[Hz]	1.04 $\times 10^{-1}$[mm^{-1}]
Representative frequency on Level 1	1.4 $\times 10^2$[Hz]	7.00 $\times 10^{-1}$[mm^{-1}]
Representative frequency on Level 2	2.3 $\times 10^2$[Hz]	
Representative frequency on Level 3	4.5 $\times 10^2$[Hz]	
Representative frequency on Level 4	8.8 $\times 10^2$[Hz]	1.2 $\times 10^0$[mm^{-1}]
Representative frequency on Level 5	1.7 $\times 10^3$[Hz]	
Representative frequency on Level 6	4.7 $\times 10^3$[Hz]	
Maximum frequency on Level 6 f_{max}	4.7 $\times 10^3$[Hz]	1.6 $\times 10^0$[mm^{-1}]

Discussion By Kolmogorov Turbulence Theory

The relation between wavelets level and wavenumber is discussed by applying Kolmogorov turbulence theory [Champman 1979] to the time axis on discrete wavelets multiresolved resolution. Kolmogorov wavenumber k_k that indicates the highest viscous dispersion rate is expressed by

$$k_k = \left(\frac{\varepsilon}{\nu^3}\right)^{\frac{1}{4}} \quad \text{——(26).}$$

Where, ν is a kinematic viscosity, ε is an energy transportation rate, that is,

$$\varepsilon = A\frac{v_0^3}{l_0} \quad v_0 = 0.2\bar{v} \quad \text{——(27)}.$$

Where, v_0 is a representative velocity fluctuation that is assumed to be 0.2 times of the mean velocity $\bar{v}$, and l_0 is a length scale in the energy contain region that is assumed to be a radius of the pipeline (=D/2). In this study, the constant A is assumed to be 1.0. The representative wavenumber on wavelets level m is obtained by

$$k_m = \frac{2\pi f_R}{v_0} \quad \text{——(28).}$$

Where, f_R is a representative frequency which is the maximum power spectrum density in Fig.4. The relation between the wavelets level and the representative wavenumber is shown in Table 2. From this table, Level 0 indicates a wavenumber under the energy contain region, and Level 6 indicates the vicinity of Kolmogorov wavenumber k_k. The wavelets level covers from the energy contain region to the viscous dispersion region.

In next, all shear stress on each wavelets level are defined by

$$\overline{\tau_{all}} = \sum_{j=1}^{512}\sum_{i=1}^{25}\sqrt{(\overline{\tau_{ij}})^2} \quad \text{——(29)}$$

to consider the relation between the stress and Re number. i is a position on the time axis, j is a position on the space axis. Fig.11 shows the results. The horizontal axis is the representative wavenumber in Table 1 normalized with Kolmogorov wavenumber k_k.

In this figure, the shear stress gets small in the energy contain region equivalent to Level 0 as Re number increases. From Fig.7(d), the slope of shear stress is steep at high Re number in the energy contain region; therefore, the value becomes small when it is normalized. On the other hand, the shear stress gets large in the viscous dispersion region equivalent to Levels 4 and 5 as Re number increases. That is because the eddy dispersion is less influenced by the viscosity in high Re number. This visualization technique is realized to be proper from the above-mentioned qualitative consideration.

Table 2 Relation between wavelets level and representative wavenumber

	v=8m/s Re=6960	v=14m/s Re=12180	v=20m/s Re=17400
Representative wavenumber on Level 0	7.7 $\times 10^{-1}$[cm^{-1}]	4.4 $\times 10^{-1}$[cm^{-1}]	3.1 $\times 10^{-1}$[cm^{-1}]
Wavenumber in energy contain region k_0	8.0 $\times 10^{-1}$[cm^{-1}]	8.0 $\times 10^{-1}$[cm^{-1}]	8.0 $\times 10^{-1}$[cm^{-1}]
Representative wavenumber on Level 1	5.4 $\times 10^{0}$[cm^{-1}]	3.1 $\times 10^{0}$[cm^{-1}]	2.1 $\times 10^{0}$[cm^{-1}]
Representative wavenumber on Level 2	9.2 $\times 10^{0}$[cm^{-1}]	5.3 $\times 10^{0}$[cm^{-1}]	3.7 $\times 10^{0}$[cm^{-1}]
Representative wavenumber on Level 3	1.8 $\times 10^{1}$[cm^{-1}]	1.0 $\times 10^{1}$[cm^{-1}]	7.1 $\times 10^{1}$[cm^{-1}]
Representative wavenumber on Level 4	3.4 $\times 10^{1}$[cm^{-1}]	2.0 $\times 10^{1}$[cm^{-1}]	1.4 $\times 10^{1}$[cm^{-1}]
Representative wavenumber on Level 5	6.7 $\times 10^{1}$[cm^{-1}]	3.9 $\times 10^{1}$[cm^{-1}]	2.7 $\times 10^{1}$[cm^{-1}]
Representative wavenumber on Level 6	1.9 $\times 10^{2}$[cm^{-1}]	1.0 $\times 10^{2}$[cm^{-1}]	0.7 $\times 10^{2}$[cm^{-1}]
Maximum wavenumber on Level 6 k_{max}	1.96 $\times 10^{2}$[cm^{-1}]	1.12 $\times 10^{2}$[cm^{-1}]	0.79 $\times 10^{2}$[cm^{-1}]
Kolmogorov wavenumber k_k	3.49 $\times 10^{2}$[cm^{-1}]	2.67 $\times 10^{2}$[cm^{-1}]	1.76 $\times 10^{2}$[cm^{-1}]

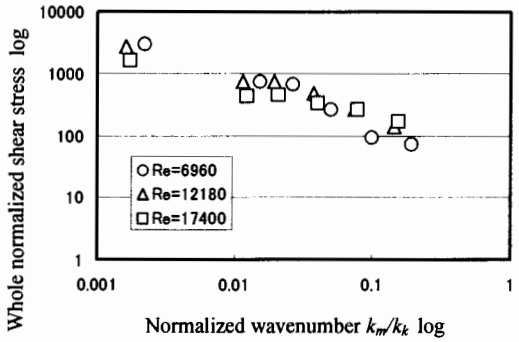

Fig.11 Relation between whole normalized shear stress and wavenumber on the time-space

CONCLUSIONS

A micro machine shear-stress imaging chip was used to measure the instantaneous shear-stress distribution in a turbulent wall boundary layer in conditions from Re number 6,980 to 17,400. The two dimensional shear stress distributions are visualized with discrete wavelets transform. As a result, the following becomes clear.

(1) Structures of wall shear stress are able to be decomposed and be clearly visualized on each frequency level without erasing time-space information.

(2) The whole shear stress on Levels 0 and 1 relevant to near energy contain region in high Re number is smaller than that in low Re number. The slope of shear stress is steep at high Re number in the energy contain region; therefore, the value becomes small when it is normalized.

(3) The whole shear stress on Levels 4 and 5 relevant to near viscous dispersion region in high Re number is higher than that in low Re number. It is reasonable because the structure is less influenced by the viscosity in high number.

ACKNOWLEDGMENTS

The authors wish to thank Dr. F. Jiang and Dr. Y.-C. Tai from the California Institute of Technology.

REFERENCES

Alfredsson,P.H., Johansson,A.V., Haritonidis,J.H. and Eckelmann,H., (1988), "The Fluctuating Wall-Shear Stress and the Velocity Field in the Viscous Sublayer", *Phys. Fluids*, 31 (5), pp.1026-1033.

Bruun,H.H., (1995), "Hot-Wire Anemometry," Oxford University Press, pp.272-286.

Champman,D.R., (1979), "Computational Aerodynamics Development and Outlook", *AIAA J.*, Vol.17, No.12, 1293-1313

Cantwell,B.J., (1981), "Organized Motion in Turbulent Flow," *Ann.Rev.Fluid Mech.*, Vol. 13, pp.457-515.

Everson,R. and Sirovich,L., (1990), "Wavelets Analysis to the Turbulence Jet", *Phys.Lett.*, Vol.145 No.6, pp314-322

Falco, R., (1980), "The Production of Turbulence Near a Wall," *AIAA Paper*, 80-1356.

Gordeyev,S.V. and Thomas,F.O., (1995), "Measurement of Reynolds Stress Reversal in a Planar Jet by Means of a Wavelets Decomposition", *Turbulent Flows ASME.* FED-Vol.208. pp.49-54

Head,M.R. and Bandyopadhyay,P., (1981), "New Aspects of Turbulent Boundary-Layer Structure," *J. Fluid Mech.* Vol.107, pp.297-338.

Horii,K., (1990), "Using Spiral Flow for Optical Cord Passing", *Mechanical Engineering-ASME*, Vol.112, No.8, pp68- 69

Ho,C.M., Tung,S. and Tai,Y.C., (1996), "Interactive Control of Wall Structures by MEMS-Based Transducers," *Advances in Turbulence, Proceedings of the Sixth European Turbulence Conference*, pp.413, Lausanne, Switzerland, July.

Ho,C.M., Tung,S, Lee,G.B., Tai,Y.C., Jiang,F. and Tsao,T., (1997), "MEMS-A Technology for Advancements in Aerospace Engineering," *AIAA Paper* 97-0545.

Huang, J.B., Tung,S., Ho,C.H., Liu,C. and Tai,Y.C., (1996), "Improved Micro Thermal Shear-Stress Sensor," *IEEE ansactions on Instrumentation and Measurement*, Vol.45, No.2, pp.570.

Jiang,F., Tai, Y.C., Gupta,B., Goodman,R., Tung,S., Huang, J.B. and Ho,C.M., (1996), "A Surface-Micromachined Shear Stress Imager," *Proceedings of the 9th International IEEE Workshop on MEMS*, p.110, San Diego.

Kim,H.T., Kline,S.J. and Reynolds,W.C., (1971), "The Production of Turbulence Near a Smooth Wall in a Turbulent Boundary Layer," *J. Fluid Mech.* Vol.50, Part1, pp.133-160.

Kim,J., Moin,P. and Moser,R., (1987), "Turbulent Statistics in Fully Developed Channel Flow at Low Reynolds Number," *J. Fluid Mech.* Vol.177, pp.133-166.

Kimura,M., et al., (1997) "MEMS for Aerodynamic Control", *28th AIAA Fluid Dynamics Conference, AIAA Paper*, 97-2118

Kimura,M., Tung,S., Lew,J., Ho,C.M., Jiang,F., Tai,Y.C.,: Measurements of Wall Shear Stress of a Turbulent Boundary Layer using a Micro-Shear-Stress Imaging Chip, Fluid Dynamics Research, Vol.24、No.6 (1999) 329-342

Li,H. and Nozaki,T., (1995), "Wavelets Analysis for the Plane Turbulence Jet (Analysis of large eddy structure) ", *JSME International Journal Fluids and Thermal Engineering*, Vol.38, No.4 pp525-531

Molet,F. et al., (1982), "Wavelets Propagation and Sampling Theory", *Geophysics*, Vol.47,pp203-236

Naqwi,A.A. and Reynolds,W. C., (1991), "Measurement of Turbulent Wall Velocity Gradients using Cylindrical Waves of Laser Light," *Experiments in Fluids*, Vol.10, pp.257-266.

Obi,S., Inoue,K., Furukawa,T, and Masuda,S.,: Experimental Study on the Statistics of Wall Shear Stress in Turbulent Channel Flows, Proceedings of 10th Symposium on Turbulent Shear Flows Vol. 1 (1995) 5-19 - 5-24.

Saito,Y., (1996), "Wavelets Analysis for Computational Electromagnetics, (in Japanese) ", *Trans. IEE of Japan,* Vol. 116A, No10, pp833-839

Smith,C.R. and Metzler,S.P., (1983), "The Characteristics of Low- Speed Streaks in the Near-Wall Region of a Turbulent Boundary Layer," *J.Fluid Mech.* Vol.129, pp.27-54.

Takei,M. et al., (1997), "Transporting Particles without Touching Pipe Wall", *ASME FED,* FEDSM97-3629

Tung,S., Hong,H., Huang,J.B., Ho,C.M., Liu,C. and Tai,Y. C., (1995), "Control of a Streamwise Vortex by a Mechanical Actuator," *Proceedings of 10th Symposium on Turbulent Shear Flows*, Vol.1, pp.1-19, Pennsylvania, USA, August.

Walker,S.H., Gordeyev,S.V. and Thomas,F.O., (1995), "A Wavelets Transform Analysis Applied to Unsteady Jet Screech Resonance", *High speed jet flow ASME.* FED-Vol.214.pp103-108

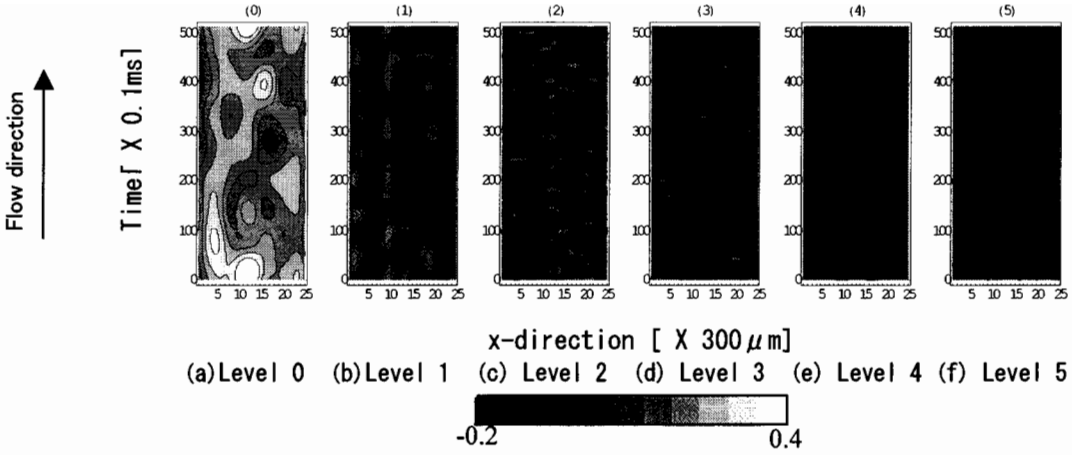

Fig. 8 Multiresolution analysis in Re=6960

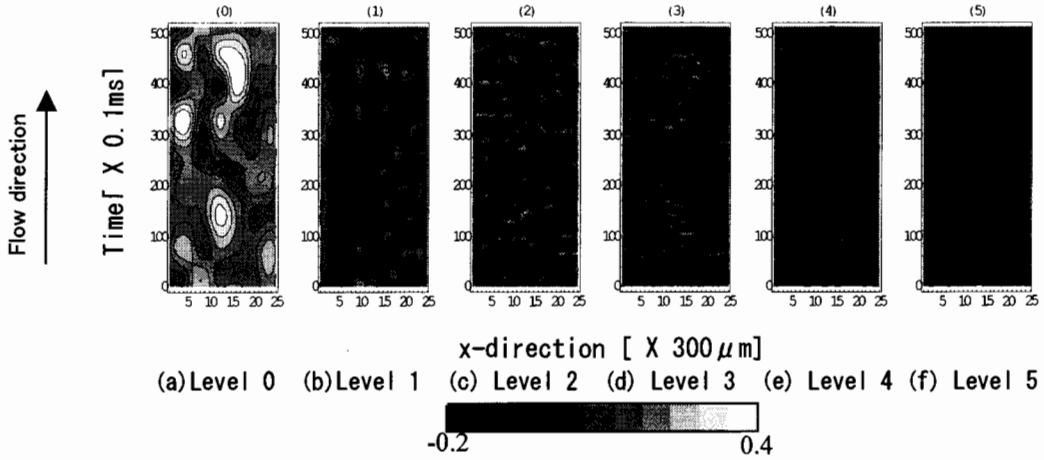

Fig.9 Multiresolution analysis in Re=12180

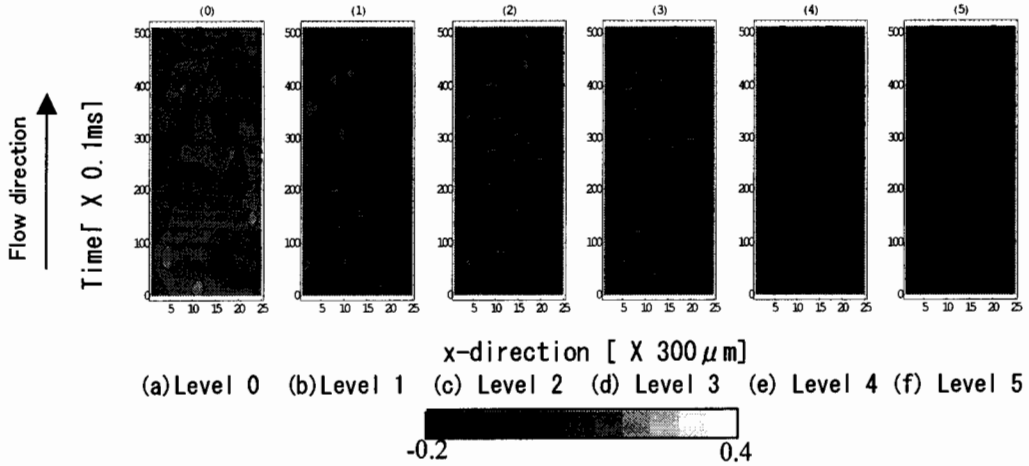

Fig.10 Multiresolution analysis in Re=17400